POLITECNICO DI TORINO
Repository ISTITUZIONALE

Spintronic Memtransistor Leaky Integrate and Fire Neuron for Spiking Neural Networks

Original
Spintronic Memtransistor Leaky Integrate and Fire Neuron for Spiking Neural Networks / Lone, A.H., Tang, M., Rahimi, D.N., Zou, X., Zheng, D., Fariborzi, H., Zhang, X., Setti, G.. - In: ADVANCED ELECTRONIC MATERIALS. - ISSN 2199-160X. - 11:13(2025). [10.1002/aelm.202500091]

Availability:
This version is available at: 11583/3017769 since: 2026-11-11T14:36:21Z

Publisher:
Wiley

Published
DOI:10.1002/aelm.202500091

Terms of use:

This article is made available under terms and conditions as specified in the corresponding bibliographic description in the repository

Publisher copyright

(Article begins on next page)

21 November 2026

Check for updates

RESEARCH ARTICLE

Editor's Choice

ADVANCED ELECTRONIC MATERIALS Open Access

www.advelectronicmat.de

Spintronic Memtransistor Leaky Integrate and Fire Neuron for Spiking Neural Networks

Aijaz H. Lone, Meng Tang, Daniel N. Rahimi, Xuecui Zou, Dongxing Zheng, Hossein Fariborzi, Xixiang Zhang, and Gianluca Setti*

Spintronic devices based on DWss and skyrmions have shown significant potential for applications in energy-efficient data storage and beyond CMOS computing architectures. Based on the ferromagnetic multilayer spintronic devices, a magnetic field-gated and current-controlled spintronic Leaky Integrate-and-Fire (LIF) neuron with memtransistor properties is showcased. The memtransistor property allows for tuning firing characteristics through external magnetic fields and current pulses. A LIF neuron model is developed based on measured characteristics to integrate the device into system-level Spiking Neural Networks (SNNs). The scalability of the neuron device is confirmed with the micromagnetic simulations in a domain-wall magnetic tunnel junction device. When integrated into SNN and convolutional SNN frameworks, the device achieves classification precision above 96%. The study highlights the device's potential as a neuron in hardware SNN architecture-based neuromorphic computing applications, combining memtransistor properties of the device and high pattern classification accuracy. The results demonstrate a promising path toward developing energy-efficient and scalable neural networks.

1. Introduction

Spintronics has shown a promising future for data storage and computing.[1,2] In particular, diverse functionalities have been explored due to tuneable physical properties in spintronic devices. Due to the different versatile device switching characteristics, Spintronics has shown remarkable presence in unconventional computing architectures like neuromorphic computing,[3–5] probabilistic computing,[6,7] and reservoir computing paradigms.[8] In particular, over the past decade, spintronic devices based on DWss (DWs), vortices, and skyrmion dynamics have been extensively pursued for applications in data storage[9] and computation.[10] The DWs and skyrmions are experimentally stabilized in a ferromagnetic thin-film system when different magnetic energy terms such as magnetic anisotropy, exchange energy, stray field energy, and Dzyaloshinskii-Moriya interaction (DMI) compete with each other to attain the energy minima. This results in a domain with all spins in the $+z$ axis and another domain in the $-z$ axis, where the two domains are connected by the DW in which the spins rotate from $+z$ to $-z$ in continuous fashion.[11] Stabilization of stripe-shaped DWss has been shown in ferromagnetic multilayer systems such as $(Co/Pt)_n$, $(CoFeB/Pt)_n$, and $(CoFeB/Ta)_n$.[12,13] These DWs are driven by the spin transfer torque STT, the spin-orbit torque SOT, or an external magnetic field. The movement of the DW creates variations in the net magnetization of the MTJ-free layer, creating an analog MTJ resistance switching characterized by the tunneling magnetoresistance TMR.[14] The domain walls and skyrmions have emerged as promising alternatives for racetrack memory,[9] neuromorphic computing,[10,15–18] and reservoir computing.[8] Especially in neuromorphic computing technologies, the magnetic DWs, and skyrmion-based magnetic tunnel junction structures have been proposed to demonstrate the synaptic and neuron behaviors in artificial neural network architectures.[3,4,19–30]

More recently, significant research in spiking neural network SNNs is gaining attention as these SNNs are considered to have better biological plausibility. Spiking Neural Networks (SNNs) are computational models that process information based on the number of spikes generated by the spiking neurons. Unlike traditional artificial neural networks that process information continuously, SNNs operate using discrete time events or spikes.[31,32] SNNs utilize spatiotemporal data encoding, giving them more energy efficiency and high performance for event-driven AI on edge computing[31–37] tasks. Some spiking

A. H. Lone, M. Tang, D. N. Rahimi, X. Zou, H. Fariborzi, G. Setti
Computer, Electrical and Mathematical Sciences and Engineering (CEMSE) Division
King Abdullah University of Science and Technology (KAUST)
Thuwal 23955-6900, Saudi Arabia
E-mail: aijaz.lone@kaust.edu.sa

D. Zheng, X. Zhang
Physical Sciences and Engineering (PSE) Division
King Abdullah University of Science and Technology (KAUST)
Thuwal 23955-6900, Saudi Arabia

The ORCID identification number(s) for the author(s) of this article can be found under https://doi.org/10.1002/aelm.202500091

© 2025 The Author(s). Advanced Electronic Materials published by Wiley-VCH GmbH. This is an open access article under the terms of the Creative Commons Attribution License, which permits use, distribution and reproduction in any medium, provided the original work is properly cited.

DOI: 10.1002/aelm.202500091

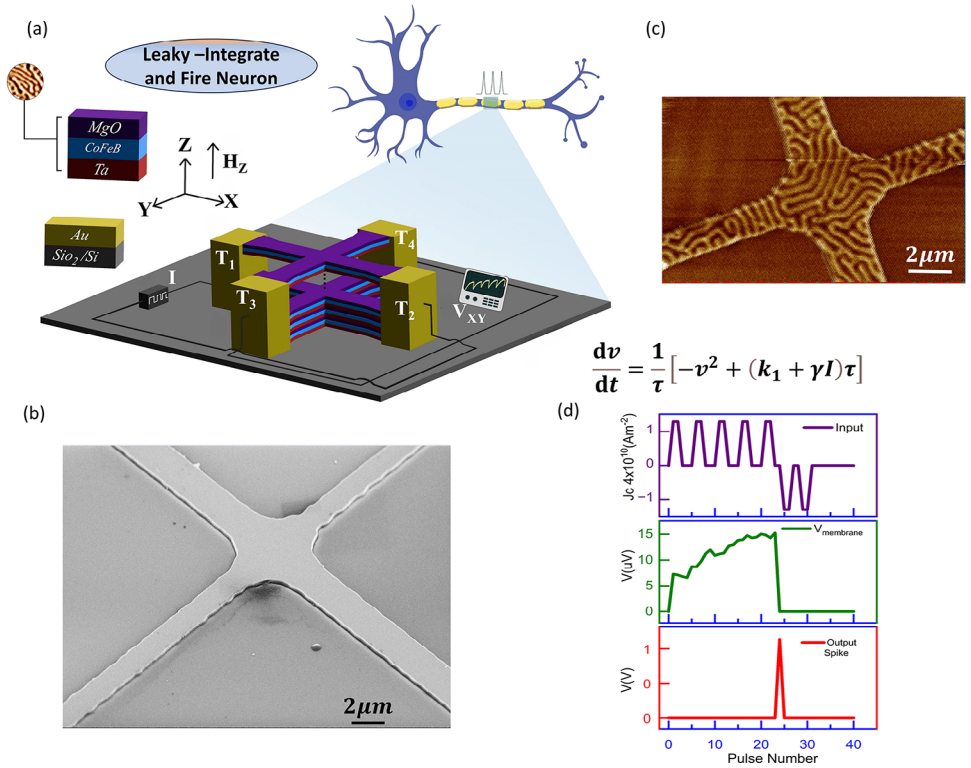


Figure 1. a) Spintronic crossbar device structure. b) Scanning electron microscopy SEM image of the device. c) Magnetic force microscopy image shows stripe domains. d) Spiking neuron characteristics of the device.

neurons have recently been proposed based on different spintronic devices. However, most of these proposals are restricted to the simulations only,[19,38,39] apart from a few experimental works,[20,40] which have shown spiking neurons -based on magnetization oscillations. However, to our knowledge, the practical realization of a spintronic memtransistor leaky integrated fire (LIF) neuron is yet to be available.

This paper experimentally demonstrates the practical realization of multilayer ferromagnetic spintronic devices exhibiting biologically inspired leaky integrate and fire neuron (LIF) behavior. These LIF neuron devices are based on the magnetic DWs or skyrmion switching in the [Ta/CoFeB/MgO]x20 ferromagnetic multilayer system. The current pulses applied laterally drive the DWs, resulting in gradual switching. The magnetic field bias is used to tune the firing characteristics of LIF neurons. We also propose a scalable micromagnetic version of the LIF device. The characteristics of the experimental/simulated neuron device are modeled as the modified LIF neuron. The models are integrated into the three-layer spiking neural network (SNN) and convolutional CSNN framework to test these spiking neurons for classifying the MNIST and FMNIST datasets. In both architectures, the network achieves classification accuracy above 96%. Additionally, the LIF neuron latency is in ns; thus, when integrated with the CMOS, the proposed device structures and associated systems exhibit an excellent future for energy-efficient neuromorphic computing.

2. Results and Discussion

2.1. Magnetic Multilayer LIF Neuron Device Structure

The multilayer spintronic LIF neuron device structure is shown in **Figure** 1a. The device structure comprises the $(Ta(2)/CoFeB(0.9)/MgO(2)) \times 20$ multilayer system, where the thickness mentioned is in nm scale. Note: The device structure in Figure 1a establishes the spintronic memtransistor neuron concept. The MgO thickness is kept at 2 nm to decouple the Hall bars from each other, which results in a configuration of parallel multiple resistors. We expect the net Hall signals to be the sum of signals from each single Hall bar. Indeed, a similar concept and results could be achieved with the metal spacer and other magnetic material systems, but in that case, Hall signals will not be decoupled from each other. Devices were fabricated as crossbars with asymmetry such that one arm is $(3 \times 50\,\mu m^2)$, while the other is $(2 \times 50\,\mu m^2)$, as shown in the scanning electron microscopy SEM image in Figure 1b. At zero field, we observe stabilization of the narrow stripe domains in the device as shown in the magnetic force microscopy MFM image (see Figure 1c). In the Ta/CoFeB multilayer systems, the chiral Neel-type stripe DWs are stabilized due to DMI, and the direction of motion depends on the sign of DMI. The current pulses are applied between terminals T-1 and T-2, which generate the spin transfer torque STT, joule heating, and small possible SOT effects in the CoFeB thin film. The joule heating in the sample also seems to play a role in switching the magnetization of the device by magnetic field-assisted

© 2025 The Author(s). Advanced Electronic Materials published by Wiley-VCH GmbH

2199160x, 2025, 13, Downloaded from https://advanced.onlinelibrary.wiley.com/doi/10.1002/aelm.202500091 by Politecnico Di Torino Sist. Bibl Del Polit Di Torino, Wiley Online Library on [11/11/2026]. See the Terms and Conditions (https://onlinelibrary.wiley.com/terms-and-conditions) on Wiley Online Library for rules of use; OA articles are governed by the applicable Creative Commons License

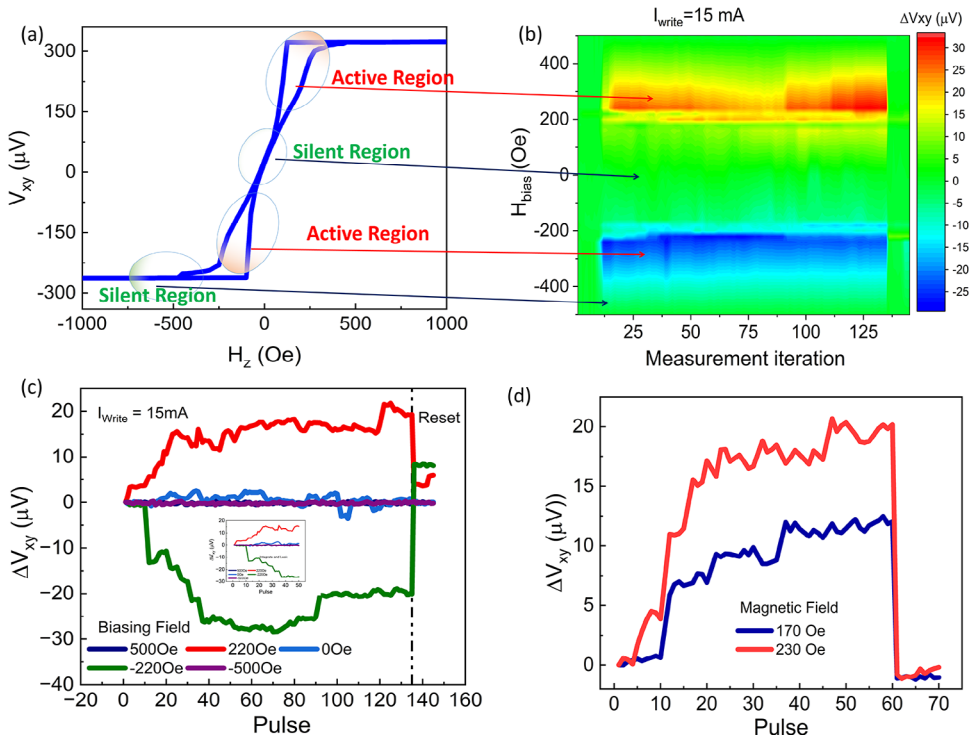


Figure 2. a) Anomalous Hall Resistance- magnetic field hysteresis characteristics showing the regions of device operation. b) The neuron output voltage (measured Hall voltage), as the function of the magnetic field and the number of current pulses (measurement iteration), show the excitatory and inhibitory regions of device operation. c) current driven field gated - LIF behavior measured at the H(− 500 *Oe*, − 220 *Oe*, 0, 220 *Oe*, and 500 *Oe*). d) LIF neuron voltage (anomalous Hall measured) following LIF behavior measured at H = 170 *Oe* and 230 *Oe*.

current-controlled DWs motion. We apply a perpendicular magnetic field to bias the magnetization of the device at a desired resistance value, which we categorize into two regions, namely excitatory and inhibitory regions. Then, using continuous current pulses ranging from 2×10^{10} Am^{-2} to 7×10^{10} Am^{-2}, the magnetization switching mimicking the integrate and leak behavior is achieved. A certain voltage threshold for firing (determined by the read OP-AM Comparator) is chosen. After spike generation, we reset the device's rest potential by a magnetic field. The integrate and leak characteristics are obtained by employing the four significant effects: 1) DWs pinning/depinning, 2) magnetic field-assisted current-driven DWs dynamics, 3) thermal effects, and 4) fabrication asymmetries in the crossbar dimensions. The observed characteristics mimic the typical leaky-integrate and fire (LIF) neuron, which is considered one of the simplified neuron models in neuroscience and used in spiking neural networks SNNs. Especially the leakage in the neuron plays a crucial role in encoding the timing information, which is essential to differentiate the old and new input spikes. Figure 1d shows the leaky integrate and fire neuron characteristics achieved by the device. Here, by applying the current pulses with density $J_c = 6 \times 10^{10}$ Am^{-2}. and biasing the device at 220 *Oe* external magnetic field. The current pulses of width 500 μs assist and magnetic field assist each other in switching the magnetization by the combination of spin transfer torque STT, thermal effects, magnetic field driven DW motion, and possible spin-orbit torque SOT can't be neglected. At $J_c = 6 \times 10^{10}$ Am^{-2}, which is 13 mA current and field 220 *Oe*, the measured anomalous Hall voltage signals increase with the current pulse, and in the absence of the current, the leaky behavior in anomalous Hall voltage is observed, as shown in Figure 1d. The read signals are compared to the fixed threshold voltage, 15 μV in this case, and a spike is generated as the voltage reaches 15 μV, as shown in Figure 1d. We furthermore model this behavior using the differential equation presented in Figure 1. The device operation and results are discussed thoroughly in the following sections.

Figure 2 explains the magnetic field gating for tuning the operating region, thus, spiking properties of the LIF neurons. The devices can be operated in two regions depending on the magnitude of the external magnetic field, as shown in Figure 2a. If the magnetic field is in the range of +150 *Oe* to 230 *Oe* or if the magnetic field range is (−230 *Oe* to −150 *Oe*), we observe evident hysteresis with a memory window. The Anomalous Hall resistance of the device depends upon its perpendicular magnetization,

$$\rho_{xy} = \rho^O + \rho^A + \rho^T = R_O B + R_S \mu_0 M_Z + R_O P B_{em}^z \quad (1)$$

The first and third terms represent ordinary Hall resistivity(voltage) and skyrmion topological Hall resistivity (voltage). These effects can be considered to have negligible contribution to net Hall voltage. Thus, only anomalous Hall dominates in our measurements. The measured output anomalous Hall voltage signals are strong, as shown in the Figure 2b heat map. The solid red region represents the output anomalous Hall voltage in (20 to 30)μV range, blue represents the output anomalous Hall voltage in (-20 to -30)μV range, and green indicates low voltage signals.

© 2025 The Author(s). Advanced Electronic Materials published by Wiley-VCH GmbH

2199160x, 2025, 13, Downloaded from https://advanced.onlinelibrary.wiley.com/doi/10.1002/aelm.202500091 by Politecnico Di Torino Sist. Bibl Del Polit Di Torino, Wiley Online Library on [11/11/2026]. See the Terms and Conditions (https://onlinelibrary.wiley.com/terms-and-conditions) on Wiley Online Library for rules of use; OA articles are governed by the applicable Creative Commons License

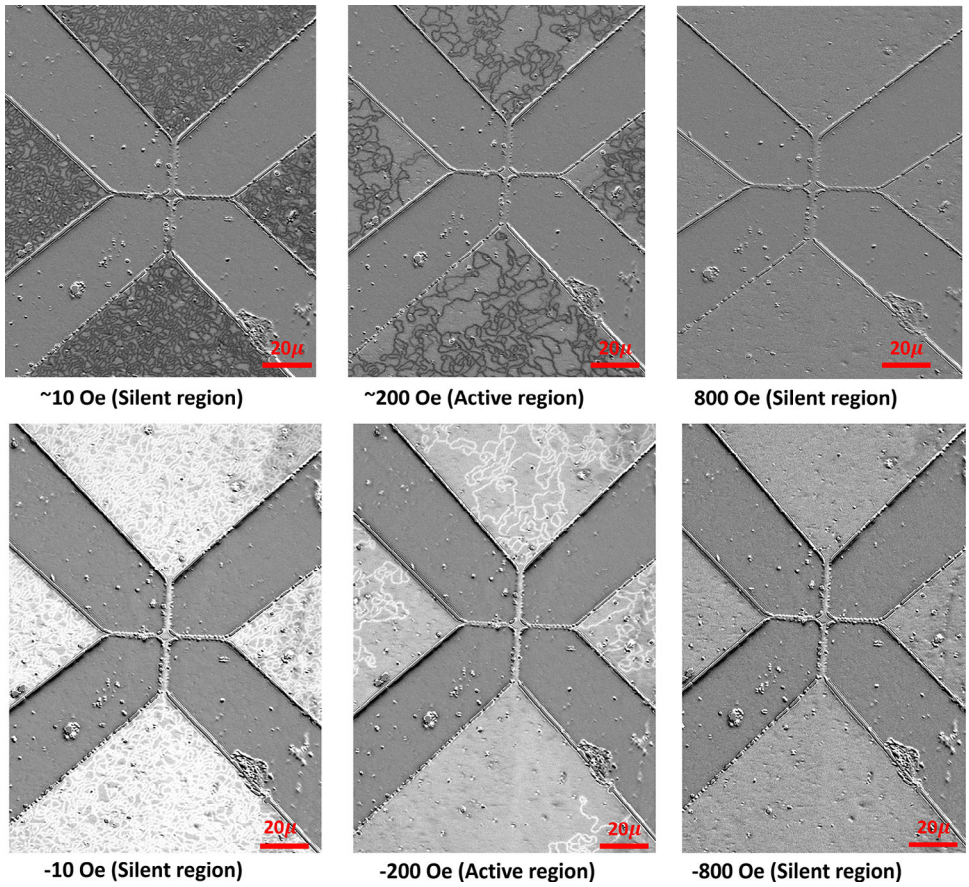


Figure 3. MOKE(differential) images of the sample at H (10 *Oe*, 200 *Oe*, 800 *Oe*, −10 *Oe*, −200 *Oe*, and −800 *Oe*.

We define this region as an active region for neuron operation. The observing of strong output anomalous Hall signals in the excitatory region is due to the available memory window for magnetization switching, as shown by the hysteresis and magneto-optical Kerr effect (MOKE) microscopy images in **Figure 3**. Once we bias the device in the active region of the hysteresis curve, the current pulses assist the magnetic field in achieving magnetization switching. Thus, anomalous Hall voltage V_{xy} is integrated. Whereas in the absence of current pulses the anomalous Hall voltage V_{xy} leakage is observed. This range is defined as the active region because the neurons working in this region have a higher probability of reaching the threshold voltage and firing. When biased in this region, the neuron device responds positively to the input current pulses (signals from other neurons); thus, the neuron is excited by other pre-neurons, which leads to a significant spiking probability in these devices. In the case of a biasing field in the range −100 *Oe* to 100 *Oe* or above or below 250 *Oe* or −250 *Oe*, the measured output voltage signals are weak (green region), indicating that the neurons working in this region find it hard to reach the threshold voltage and fire. Thus, these neurons have very low spiking probability, as shown in Figure 2c. The neurons biased in this region are defined as silent neurons, or this region is called a silent region. In the case of the silent region, as observed in the hysteresis loops and clearly shown in the MOKE images at (+10 Oe, +800 Oe, −10 Oe, and −800 Oe), the existence of the almost equal number of up and down domains makes the $M_z = 0$. The hysteresis curves are pinched in a specific range, indicating no memory window or very difficult current-controlled switching due to complex interactions among the up and down domains. This results in negligible V_{xy} switching in (-100 to 100) Oe. The reason behind this is the cancellation of the field-assisted STT due to many magnetic domains that don't allow any DWs motion/expansion. In the saturation range (MOKE images at −800 Oe and +800 *Oe*), the magnetization is saturated either in positive M_z or $-M_z$. The ratio of $+z/-z$ or $z/+z$ domains is 1 as shown in hysteresis and MOKE; thus, no room for magnetization switching in the region is observed, as seen in the V_{xy} obtained above 250 *Oe* or below −250 *Oe* field. The magnetic layers act like a large single domain, so there is no DWs; hence, DWs motion and expansion are very unlikely. resulting in minute voltage switching which makes the probability of firing these neurons very low. In the active region, the ratio of $+z/-z$ or $z/+z$ domains is less than 1 as shown in hysteresis, such as for H(200 *Oe*), the +z (up) domain size dominates. So, there is room for domain expansion/contraction. With the applications of the current pulses, the multiple effects such as magnetic field, STT, SOT (negligible), and Joule heating collectively work to allow further DWs motion/expansion, as seen in the increased V_{xy} with current pulses. Similarly as shown in Figure 2 and MOKE images (Figure 3) there is room for domain expansion/contraction which allows the larger voltage switching as observed in the H(− 200 *Oe*) region.

 © 2025 The Author(s). Advanced Electronic Materials published by Wiley-VCH GmbH

2199160x, 2025, 13, Downloaded from https://advanced.onlinelibrary.wiley.com/doi/10.1002/aelm.202500091 by Politecnico Di Torino Sist. Bibl Del Polit Di Torino, Wiley Online Library on [11/11/2026]. See the Terms and Conditions (https://onlinelibrary.wiley.com/terms-and-conditions) on Wiley Online Library for rules of use; OA articles are governed by the applicable Creative Commons License

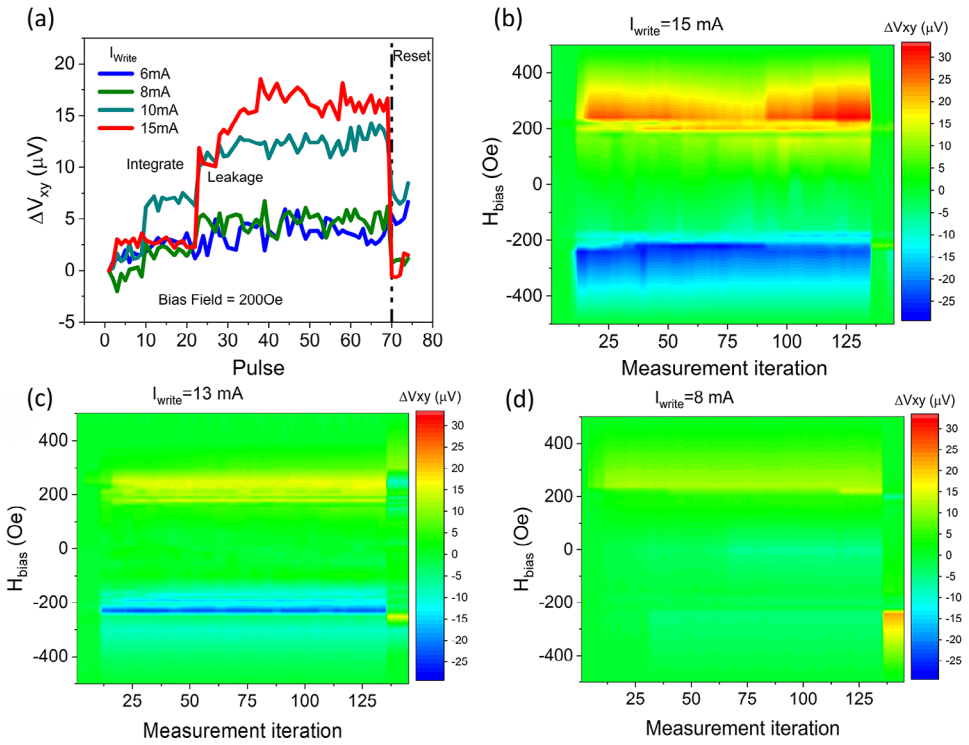


Figure 4. a) LIF voltage characteristics at constant field 200*Oe* and write current (6 , 8 , 10 , and 15 mA). LIF voltage signal is a function of the magnetic field and current pulses (measurement iteration) for different write current amplitudes. b) 15 mA, c) 13 mA, d) 10 mA, and Magnetization evolution with current (simulation) (e1) Magnetization profile, and (e2-e4) Magnetization texture.

Moreover, we have added the current controlled magnetization evolution micromagnetic simulations of a *Ta*/*CoFeB*/*MgO* Hallbar device at magnetic fields −220 *Oe*, −10 *Oe*, and 220 *Oe*, which show how current pulses help the field-assisted DW motion or expansion, as shown in Figure S3 (Supporting Information). We observe significant domain expansion at −220 *Oe* and +220 *Oe*, such that the Hallbar magnetization reaches almost saturation, whereas no such behavior is observed in the −10 *Oe* field see Figure 2e. The anomalous Hall voltage is directly proportional to the z component of the magnetization. As shown in Figure S2 (Supporting Information), the magnetization profile indicates that current-assisted switching dominates at −220 *Oe* and +220 *Oe* more than at −10 *Oe*. Thus, these images also explain the different device characteristics observed in excitatory and inhibitory regions. The magnetic field-gated current-controlled output voltage results demonstrate that the device behaves like a spintronic neuron with transistor properties or memtransistor LIF neurons. Here, the external magnetic field is working analogous to the MOSFET gate voltage. This plays an important role in the circuit-level implementations where the crossbars -based on these devices can be realized. The concept is further demonstrated in Figure 2c, for the writing current equal to 15 mA (6.5×10^{10} Am^{-2}) and varying magnetic biasing field. We observe that the output leaky-integrated voltage signals are maximum (20 μV) for $H = +220$ *Oe* and (−30 μV) for −220Oe. Whereas, for $H = 0$ *Oe*, 500 *Oe*, and − 500 *Oe*, the voltage is relatively 0. This behavior shows no response to the current pulses in this region and demonstrates the inhibitory property shown by the device. Finally, after reaching the threshold voltage, the resetting of the neuron to a resting potential is achieved by applying a resetting field. Note: In Figure 2c pulses onward number 60 are not required as no further significant switching is obtained, so, Figure 2d shows the LIF characteristics in which resetting is done at pulse (iteration) number 60. As shown last section the need for the access transistor in the memory crossbar array can be avoided using this concept of spintronic memtransitor LIF neuron devices.

Figure 4 shows the magnetic field-assisted LIF neuron characteristics for different writing currents. In Figure 4a, we show the measured LIF behavior at fixed bias 200 *Oe* and writing current 6, 8, 10, and 15 mA. We observe the strongest amplitude Hall voltage signal around 22 μV for 15 mA. The output voltage signal amplitude is reduced as the writing current is lowered. Furthermore, the integration and leakage behavior becomes less noisy due to reduced DWs pinning/depinning at low writing currents compared to abrupt pinning/depinning at 15 mA. Figure 4b–d shows the output signals at different magnetic biases and current pulses in the heat-map form. It can be seen clearly that the best regions for excitatory device operations are obtained at writing current 15 mA and magnetic field bias range 180 *Oe* to 280 *Oe* [positive active region-red] and −200 *Oe* to −300 *Oe* [negative active region-blue]. As we lower the current, the output voltage starts diminishing, and the range of possible bias points is also reduced as seen in Figure 4d. Compared to the 15 mA write current, the signal amplitude at 8 mA is reduced significantly, as shown in Figure 4d. The measured results shown in Figure 4 are supported by the micromagnetic simulation shown in the supplementary material Figure S3 (Supporting

© 2025 The Author(s). Advanced Electronic Materials published by Wiley-VCH GmbH

2199160x, 2025, 13, Downloaded from https://advanced.onlinelibrary.wiley.com/doi/10.1002/aelm.202500091 by Politecnico Di Torino Sist. Bibl Del Polit Di Torino, Wiley Online Library on [11/11/2026]. See the Terms and Conditions (https://onlinelibrary.wiley.com/terms-and-conditions) on Wiley Online Library for rules of use; OA articles are governed by the applicable Creative Commons License

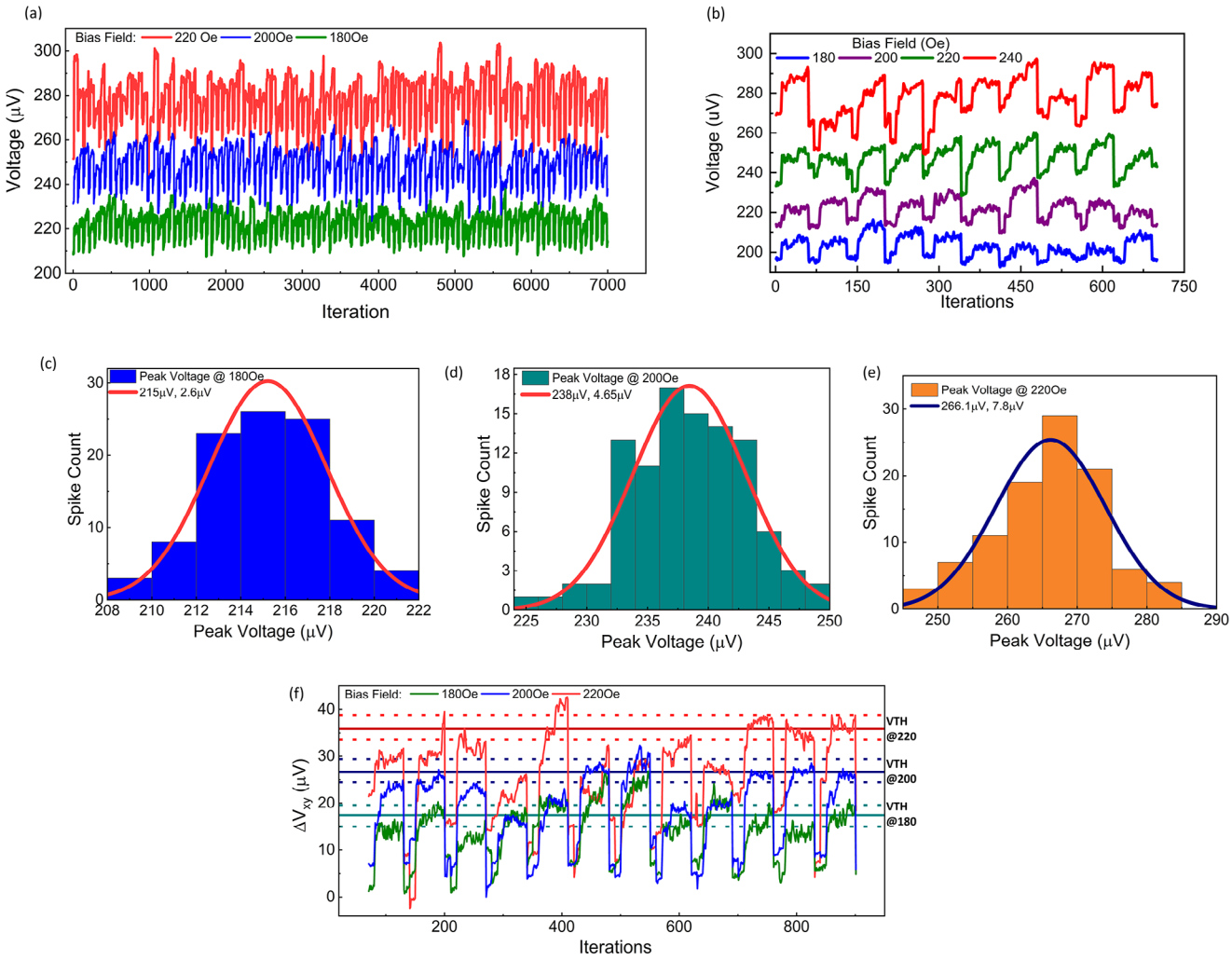


Figure 5. a) LIF characteristics for bias field 180, 200, and 220 *Oe* repeated 100 times. b) In situ LIF characteristics for bias field 180, 200, 220, and 240 *Oe* repeated ten times. Peak voltage distribution c) 180 *Oe* [$\bar{V} = 215\,\mu V$, $\sigma = 2.6\,\mu V$] d) 200 *Oe* [$\bar{V} = 238\,\mu V$, $\sigma = 4.65\,\mu V$] and e) 220 *Oe* [$\bar{V} = 266.1\,\mu V$, $\sigma = 7.8\,\mu V$]. f) Threshold voltage ranges from 180, 200, and 220 *Oe*.

Information). As shown in Figure S3 (Supporting Information), the magnetization switching in the Hall bar is enhanced by increasing the writing current. These results discussed in Figures 2, 3, and 4 demonstrate the memtransistor property of the device. By having this transistor-like capability where the magnetic field gating works like the gate voltage in a transistor and the write current between T-1 and T-2 acts like source-drain voltage. Note: The neuron characteristics (experimental) show some fluctuations. Still, this is not the electrical noise, as we have done several controlled measurements to ensure device behavior is coming from the magnetization switching. Noise doesn't depend on the magnetic field, as our measurements show. The fluctuations are expected due to multi-domain switching and the fabricated structure's DWs pinning/depinning. The measured noise levels (corresponding to no writing) shown in the Figure S1 (Supporting Information) are very small compared to when current pulses were applied. These measurements were carried out as control experiments to ensure device characteristics are not dominated by noise. Additionally, The anomalous Hall signals are usually small (in μV) range as compared to the MTJ TMR reading (mV). Here to demonstrate the concept at the device level (experimentally), we adopted anomalous Hall reading as a feasible option for reading. However, we have certainly proposed the MTJ version of a similar concept in the micromagnetic section for enhanced device geometry and output voltage scaling.

In any spiking neural network, the information is encoded majorly in neurons' spiking frequency. In **Figures 5** and **6**, we analyze the control of the spiking probability of the LIF neurons using magnetic field biasing and writing current. Figure 5 shows the variability in the device behavior at different magnetic biases. Figure 5a shows the LIF behavior executed 100 times by the device in a continuous measurement setting. We applied 10 writing current pulses for 1 LIF operation; the neuron state is read four times between two consecutive writing pulses. Once the neuron voltage reaches a certain peak (threshold), we reset the neuron using an external magnetic field. The process was repeated 100 × to estimate the mean peak voltage and the variance

© 2025 The Author(s). Advanced Electronic Materials published by Wiley-VCH GmbH

2199160x, 2025, 13, Downloaded from https://advanced.onlinelibrary.wiley.com/doi/10.1002/aelm.202500091 by Politecnico Di Torino Sist. Bibl Del Polit Di Torino, Wiley Online Library on [11/11/2026]. See the Terms and Conditions (https://onlinelibrary.wiley.com/terms-and-conditions) on Wiley Online Library for rules of use; OA articles are governed by the applicable Creative Commons License

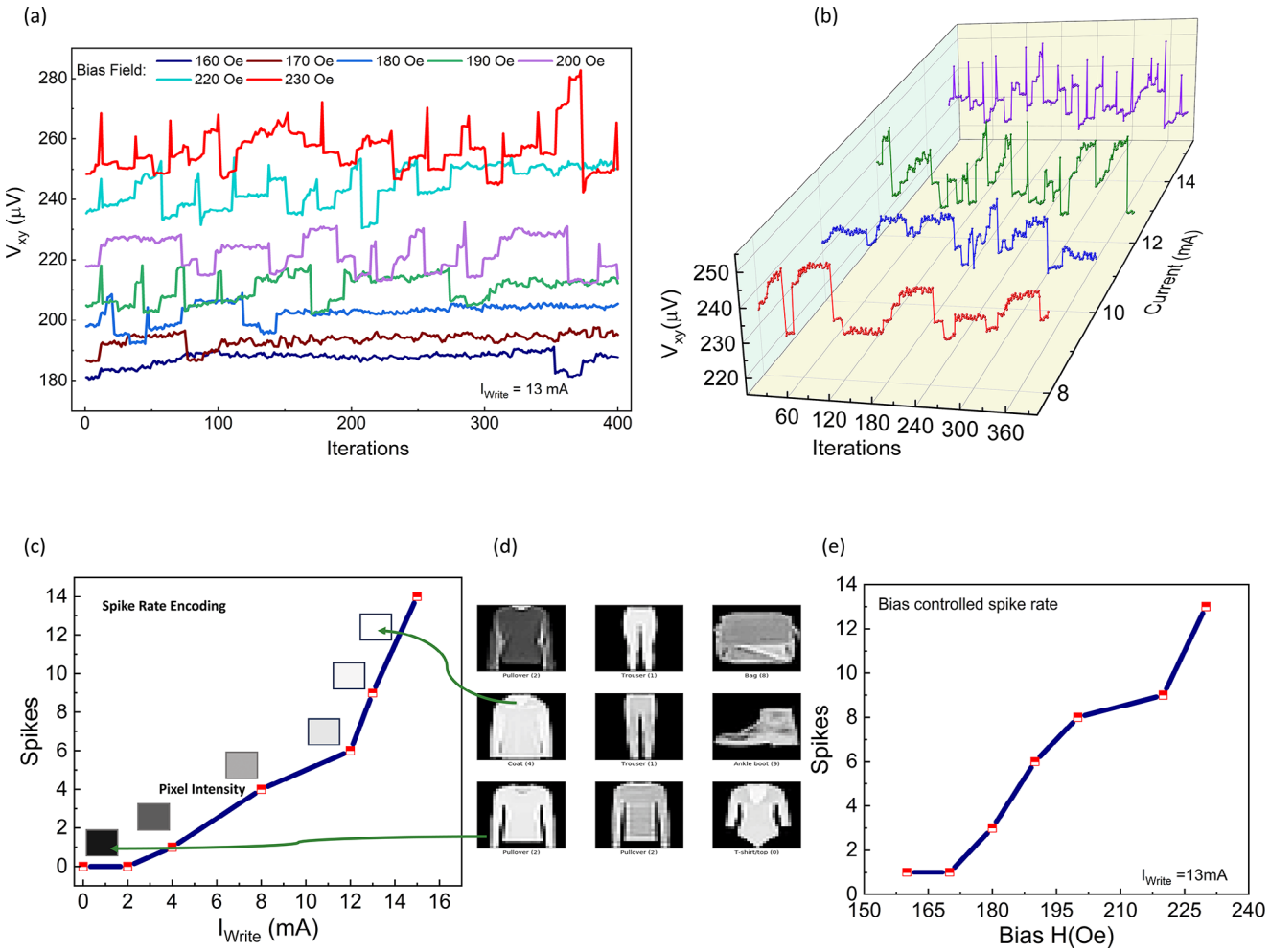


Figure 6. a) Magnetic field controlled spike rate encoding at fixed current.b) Current controlled spike rate encoding at 8, 10, 13, and 15 mA. The fashion-MNIST dataset image encoding. c) Pixel intensity is encoded into the current controlled spike rate, and d) Magnetic field controlled spike rate.

due to random DWs pinning/depinning, as shown in Figure 5a. We observed reliable neuron LIF characteristics followed by neuron reset throughout the 100 cycles. Figure 5b shows the LIF device characteristics at the bias field: 180, 200, 220, and 240; for up to 700 iterations. The neuron is reset back to a resting voltage in the proximity of 0 V (−2 μV to 2 μV) approximately. In the repeated LIF and resetting of the device, we observe fluctuations in peak voltage, which is attributed to the stochastic domain pinning/depinning in a large-area device. We expect this stochasticity to be minimized in smaller-dimension devices. The variations in peak voltage and resting voltages for different biasing points are analyzed statistically, as shown in Figure 5c–e. Figure 5c shows the peak voltage distribution at bias field 180 Oe; the mean peak voltage is 215 μV with a slight standard deviation of about 2.6 μV. Likewise, for 200 *Oe*, the mean peak voltage is 238 μV, and the deviation is 4.6 μV. For 220 *Oe*, the mean is 266.1 μV, and the standard deviation is 7.8 μV. These results indicate that the device performance is best around the biasing field $H = 180$ *Oe*. We define a range of thresholds for the actual circuit realization to overcome the mild deviations in the peak voltages. A hysteretic comparator working in the respective range will generate a spike whenever the device voltage lies in the threshold voltage range. Likewise, the device is assumed to be in complete rest if the read voltage is in the resting range. In the case of ideal reset conditions, we measure integrated leaky behavior from the device and post-process the data in ex-situ conditions. We set a voltage threshold as a comparator, which generates spikes. As shown in Figure 5f, for the magnetic field 180 *Oe*, the threshold voltage is set at 17 μ*V*, With the application of the writing current pulses, the voltage increases in LI behavior. As the voltage reaches the V_{TH} range $V_{TH} = 17 \pm 2.6\,\mu V$, the comparator (simulation) generates an output spike, and at the same time, the devices are reset back to their initial position. Likewise for 200 *Oe* and 220 *Oe* the threshold voltage ranges are ($V_{TH} = 28 \pm 4.65\,\mu V$), and $V_{TH} = 37 \pm 7.8\,\mu V$). Figure 6 shows the spintronic neuron device's magnetic field and current-controlled spike rate encoding capabilities. Figure 6a shows LIF characteristics at different bias fields in the active region (160 to 230 *Oe*). At the fixed writing current of 13 mA, the spike rate increases with bias till the 230 *Oe* field, as shown in Figure 6a,d. The resulting condition is met by assuming the same net voltage change for each bias point. Figure 6b shows LIF characteristics at bias field 200 *Oe* and writing current 8, 10,

© 2025 The Author(s). Advanced Electronic Materials published by Wiley-VCH GmbH

2199160x, 2025, 13, Downloaded from https://advanced.onlinelibrary.wiley.com/doi/10.1002/aelm.202500091 by Politecnico Di Torino Sist. Bibl Del Polit Di Torino, Wiley Online Library on [11/11/2026]. See the Terms and Conditions (https://onlinelibrary.wiley.com/terms-and-conditions) on Wiley Online Library for rules of use; OA articles are governed by the applicable Creative Commons License

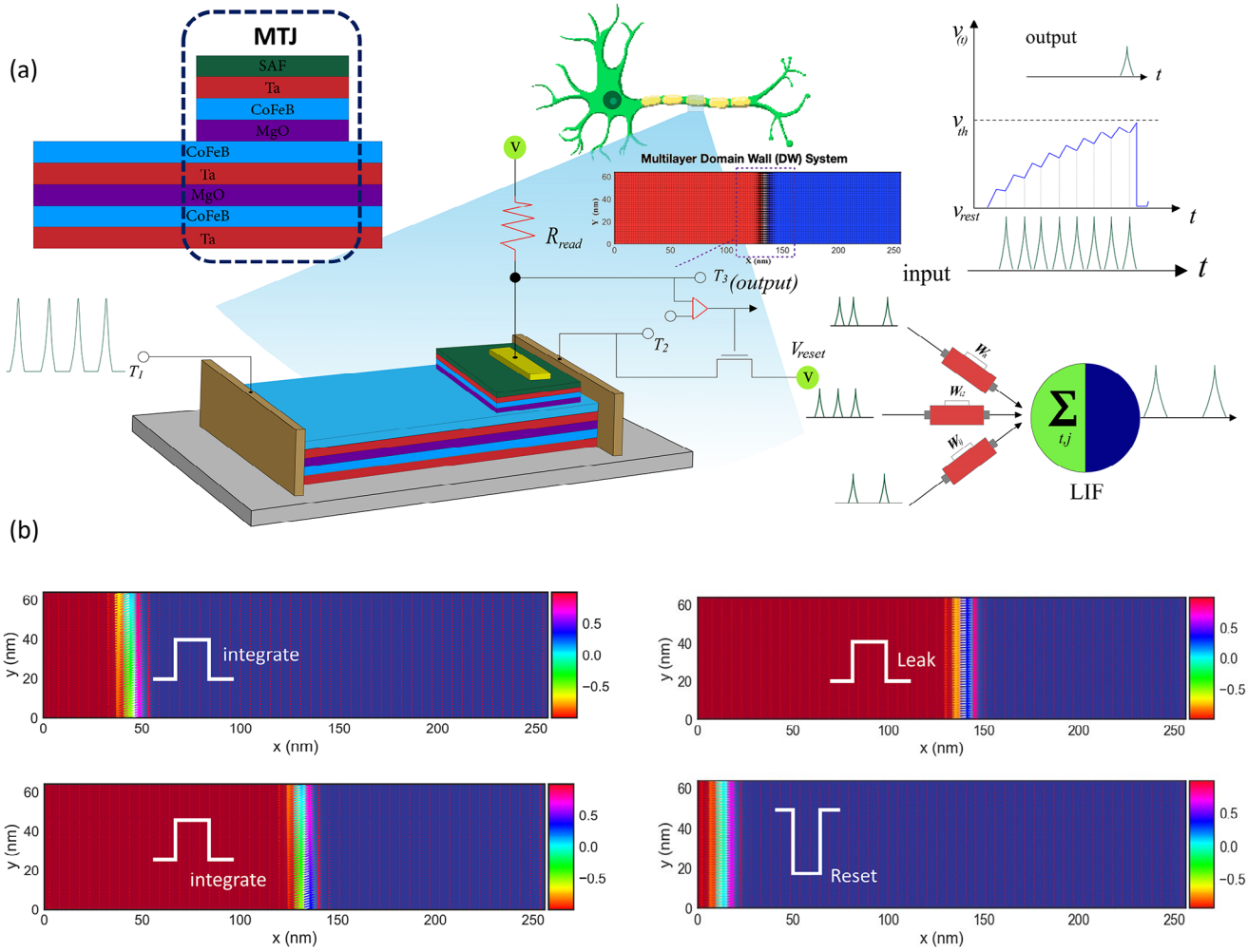


Figure 7. a) Multilayer Spintronic LIF Magnetic tunnel junction device (Micromagnetics). b) Magnetization evolution throughout the LIF process.

13, and 15 mA. The threshold voltage is fixed at 242 μV while the measurement is carried out for 400 iterations. For 8 mA current, the voltage crosses the threshold four times during the 400 iterations; for 10 mA, it crosses six times likewise, on increasing the current, the LI behavior is fast, and we obtained about 14 spikes for the writing current 15 mA. In Figure 6b, we show the images of the Fashion MNIST dataset to illustrate the spike rate encoding functionality of the device. We encode the pixel intensity from full dark to full bright into the spiking rate, as shown in Figure 6c. If the neuron receives a pixel value corresponding to dark intensity, the current going into the neuron is very small <2 mA; as the brightness increases, the current increases in proportion, and the neuron spiking rate also increases, as shown in Figure 6c. So, in the presented neuron devices, the magnetic field, and the writing current amplitude can control the spiking rate of the neuron device. This increases the device's functionality and its significance in hardware SNN implementations. Note: The device structure in Figure 1a establishes the spintronic memtransistor neuron concept. Indeed, a similar concept and results could be achieved with the metal spacer and other magnetic material systems.

2.2. Micromagnetics

To study the scalability of the presented spintronic neurons, we propose the ($256 \times 64\,nm^2$) spintronic LIF neuron device structure. The device structure consists of the (Ta/CoFeB)xn multilayer nanotracks in which either DWs or skyrmions can be moved from one end (T_1) to the other (T_2) as shown in **Figure 7a**. The SOT generated from the laterally flowing charge current drives the DW toward (T_2). The writing is done by applying current amplitude pulses $1 \times 10^{11}\,Am^{-2}$ and width 1 ns. To study the frequency response, period T varies from 1.5 to 4 ns. The neuron membrane potential (magnetization) reading is carried out by the tunneling magneto-resistance TMR effect via an MTJ reading block, as shown in Figure 7a. The changing magnetization under the reading block changes the tunneling resistance of the MTJ. Figure 7b shows the DW motion in the free layer at different operating instants. As the DW moves, it faces an increasing demagnetization energy opposing the DW motion. The reading of magnetization is done using the MTJ placed near the T_2 end of the nano-track; the presence of the current integrates the magnetization, whereas the magnetization leaks (DW moves back) in

© 2025 The Author(s). Advanced Electronic Materials published by Wiley-VCH GmbH

2199160x, 2025, 13, Downloaded from https://advanced.onlinelibrary.wiley.com/doi/10.1002/aelm.202500091 by Politecnico Di Torino Sist. Bibl Del Polit Di Torino, Wiley Online Library on [11/11/2026]. See the Terms and Conditions (https://onlinelibrary.wiley.com/terms-and-conditions) on Wiley Online Library for rules of use; OA articles are governed by the applicable Creative Commons License

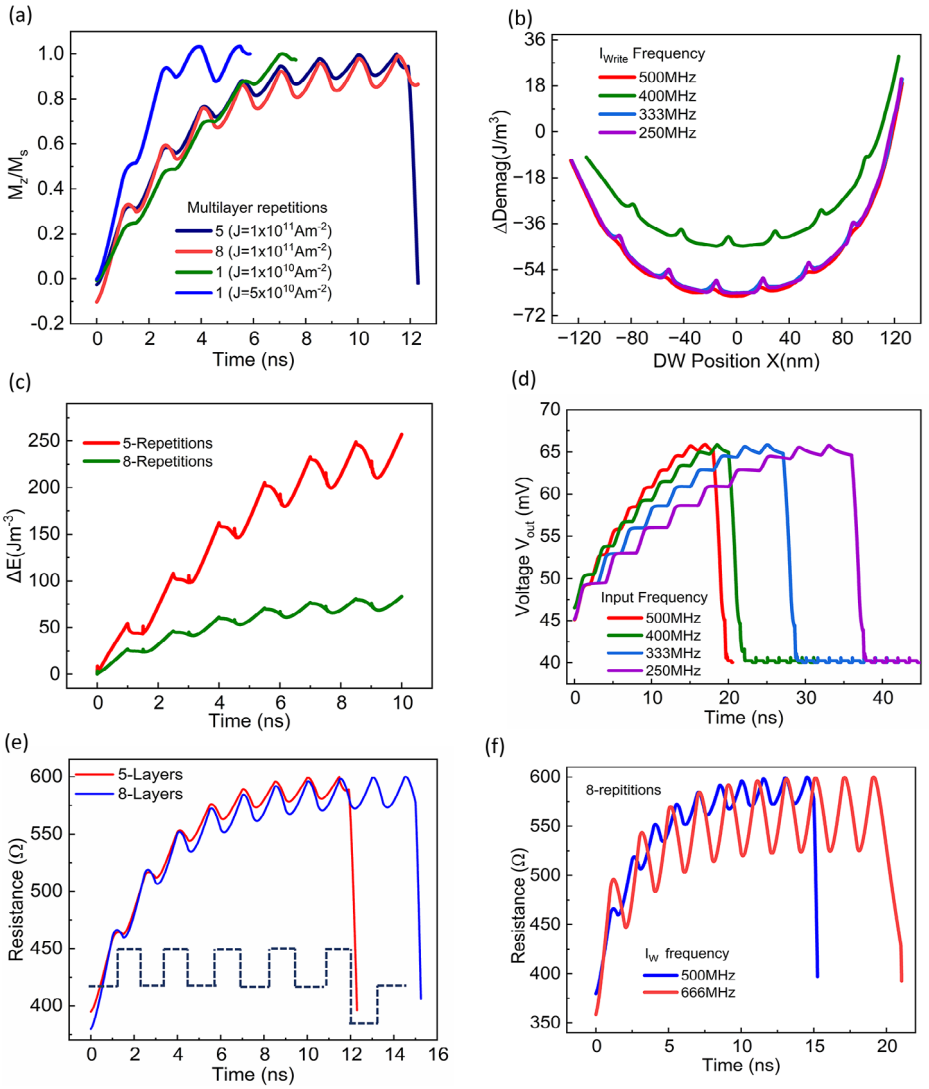


Figure 8. a) Magnetization switching in devices with multilayer repetitions 1, 5, and 8 repetitions in the presence of current pulses. b) Demagnetization energy as a function of DWs position. c) Total magnetic energy change evolving shows LI behavior. d) Multilayer DW-LIF neuron output voltage at 500, 400, 333, 250*MHz*.e) DW-LIF neuron tunnel resistance for five and eight-layer devices. f) DW-LIF neuron resistance at 500 and 666*MHz* for device with eight-repetitions.

the absence of the current due to the opposing forces. The MTJ output terminal T_2 is connected to the comparator (simulation), generating output spikes propagating to the next layer. After each spike, a negative resetting current pulse resets the membrane potential. As the membrane potential reaches the threshold voltage V_{th}, the comparator generates spikes and, at the same time, activates the resetting MOSFET, which allows a resetting current pulse in the opposite direction. This current pulse forces the DW back to its original state, and membrane potential is reset to resting potential V_{rest}.Note: We initialize the DW at the center and then move it towards the right end while it follows the LI behavior as shown. We can also put the reading MTJ on the left end of the magnetic layer, then change the current direction and realize the same behavior.

In **Figure 8**, we show the different electrical and magnetic characteristics of the DW LIF neuron device. Figure 8a shows the input current response of the proposed devices with multilayer repetitions of one, five, and eight layers, respectively. Significant magnetization leakage is obtained in devices with eight layers, followed by five layers. Although the magnetization switches much faster in the single magnetic layer device, even on reducing the writing current to 1×10^{10} Am^{-2}, the device behavior doesn't provide a reasonable leakage property needed for the LIF realization. Thus, reasonable magnetic layer repetition is essential for realizing the leaky property. As the DW moves toward the terminal T_2, a DW is initiated at −200 nm from the center towards the left. Thus, the multilayer thin film is magnetized 70% down (−z direction) and about 30% up (+z direction). The demagnetization energy is high, but as the DW starts moving right towards the center, the demagnetization is reduced until the DW reaches the center where domain sizes are equal; thus, demagnetization is minimal. The demagnetization increases further as the DW

© 2025 The Author(s). Advanced Electronic Materials published by Wiley-VCH GmbH

2199160x, 2025, 13, Downloaded from https://advanced.onlinelibrary.wiley.com/doi/10.1002/aelm.202500091 by Politecnico Di Torino Sist. Bibl Del Polit Di Torino, Wiley Online Library on [11/11/2026]. See the Terms and Conditions (https://onlinelibrary.wiley.com/terms-and-conditions) on Wiley Online Library for rules of use; OA articles are governed by the applicable Creative Commons License

2199160x, 2025, 13, Downloaded from https://advanced.onlinelibrary.wiley.com/doi/10.1002/aelm.202500091 by Politecnico Di Torino Sist. Bibl Del Polit Di Torino, Wiley Online Library on [11/11/2026]. See the Terms and Conditions (https://onlinelibrary.wiley.com/terms-and-conditions) on Wiley Online Library for rules of use; OA articles are governed by the applicable Creative Commons License

continues its motion toward the terminal T_2 as shown in Figure 8b. The scaling of the demagnetization energy with the DW position, as shown in Figure 8b, indicates the DW's most stable position to be the center of the ferromagnetic layer; thus, the energy minima are observed at the center where net magnetization $Mz = 0$. Moreover, Figure S2 (Supporting Information) shows increasing demagnetization as the function of magnetization for four different input pulse/spike frequencies. We observe two components in the demagnetization time characteristics: 1) the application of current increases the demagnetization due to the SOT on the DW spins, which are forced from the stable in-plane direction to a perpendicular direction momentarily. When the current switches back to zero, the demagnetization also relaxes, but due to DW motion, the ratio of the +z/−z domain spins changes. This gives rise to a shift in the demagnetization curve. Thus, we observe (1) a Transient volatile memory effect due to current and (2) a Stable non-volatile memory effect due to asymmetry in domain sizes. For a 50% duty cycle, a 1ns ON current followed by a 1ns OFF current pulses are applied, which means (500 MHz) input frequency; likewise, for a 40% duty cycle, the ON current pulse width is 1ns followed by 1.5 ns OFF state (400 MHz) input frequency, for a 33% duty cycle (1 ns ON/2 ns OFF), the input frequency is 333 MHz and for 250 MHz (the pulse scheme is 1 ns ON/3 ns OFF). The DW reaches the threshold position in 16 ns, and we observe no further increment in the demagnetization energy. For 333 MHz, the threshold location is achieved at around 27 ns. The demagnetization characteristics directly affect the overall motion of the DW. As the DW approaches terminal-T_2, it begins to see an increasing demagnetization force acting on it. The DW moves right in the presence of the SOT pulse, as shown in Figure 7b, but when the current is switched off, the demagnetization force starts dominating the overall motion; thus, we observe the DW moving back, as seen in Figure 7b. Thus, the current integrates the magnetization, while demagnetization opposes the current. This interplay results in a LI behavior.

Note: The effects on DW motion due to many experimental imperfections or intrinsic effects of DW pinning/depinning could not be added to the simulations. So, the results are much smoother than observed in the measurements, which include all the effects such as domain pinning/depinning, thermal effects, and fabrication imperfections that will add to the behavior, especially minor fluctuations. As explained in the previous section, the DW motion changes the net magnetization of the MTJ-free layer. Figure 8c shows the time evolution of the net change in magnetic energy during device operation. We observe the LI behavior followed by the energy profile, attributed to the free layer energy dependence on the DW position. In Figure 8d, the neuron output voltage V_{out}-time characteristics clearly show the integrate and leak behavior. The voltage is computed using Equations (1) and (2). For high input frequency (500 MHz), the normalized magnetization (Mz/Ms) reaches the threshold value of 0.9 much earlier than the other two cases. In the case of lower frequencies, such as 333 MHz, the DW gets enough time to relax; thus, magnetization leakage is increased, reflected in the blue curve. The MTJ reads the magnetization change in terms of its tunnel magnetoresistance. The magnetic tunnel junction (MTJ) characteristics, as shown in Figure 7c,d, depend on the number of repetitions (Ta/CoFeB/MgO) and current pulse amplitude. In Figure 8d, with 15 repetitions and a current pulse amplitude of 5 $\times 10^{11}$~Am^{-2}, the DWs (DW) velocity is initially fast. Still, it decreases with subsequent pulses as leakage increases, as evident from Figure 8d. This decrease in velocity allows for more relaxation time for the DW, leading to more significant leakage. In contrast, Figure 8f shows the frequency dependence of neuron resistance in a device with 8 FM repetitions and a reduced current pulse amplitude of 1×10^{11}~Am^{-2}. As expected, we observe more significant leakage starting earlier than the Figure 8d case due to the lower DW velocity at this reduced current amplitude, allowing| for more relaxation time.

The magnetization is mapped to the MTJ resistance or neuron resistance by

$$R_{\text{neuron}} = R_{\text{AP}} \frac{\left[1 - \hat{m} \cdot \hat{m}_P\right]}{2} + R_{\text{P}} \frac{\left[1 + \hat{m} \cdot \hat{m}_P\right]}{2} \tag{2}$$

here, the $R_{\text{P}}/R_{\text{AP}}$ represents the MTJ resistance in a parallel/anti-parallel state. Figure 8e shows the neuron resistance switching for two devices with five and eight layers of CoFeB. We considered the TMR 200% and $Rp/RAP = 200/600$. If the complete magnetization switching is regarded as the out switches in the range (40 to 70)mV are shown in Figure 8d. The resistance increases from 380 to 590 Ω in a leaky integrated behavior. We observe fast DW switching for the L_5 case, whereas the DW velocity is reduced for the L_8 case. Thus, the threshold voltage is achieved in 15 ns. Also, for increased CoFeB layers, the leakage conductance is increased due to increased demagnetization energy, as shown by the eight-layer resistance and MTJ neuron voltage characteristics in Figure 8e,f. The MTJ $\mathbf{T}_3$.

$$V_{\text{out}} = \frac{R_{\text{neuron}}}{R_{\text{neuron}} + R_{\text{read}}} V_{\text{read}}, \quad V_{\text{out}} \geq V_{\text{th}} : \text{spike} = 1 \quad \text{else} : \text{spike} = 0 \tag{3}$$

The output of the MTJ neuron (terminal T_3) is connected $\mathbf{T}_3$ to a voltage comparator having threshold voltage V_{th}. As the MTJ neuron voltage reaches this threshold voltage V_{th}, the comparator generates the output spikes propagating to the next layer. During firing, the reset MOSFET is also switched, allowing a current to follow from T_2 to T_1, thus driving the DW back to the initial position corresponding to resetting the neuron membrane voltage to its rest voltage.

To utilize the magnetic field gating at the circuit level, we propose the schematic shown in Figure S4 (Supporting Information).

3. Multilayer Spintronic LIF Neuron in Spiking Neural Networks

The LIF neurons are the fundamental units of the spiking neural networks, which involve thousands or millions of these units. To evaluate the prospects for the circuit-level integration of these fabricated and proposed neurons. We developed compact behavioral models describing the LIF- characteristics in these devices. We obtain the differential equation of the DW position by fitting the micromagnetic computed DW velocity with an analytical MATLAB model (more details in supplementary material

 © 2025 The Author(s). Advanced Electronic Materials published by Wiley-VCH GmbH

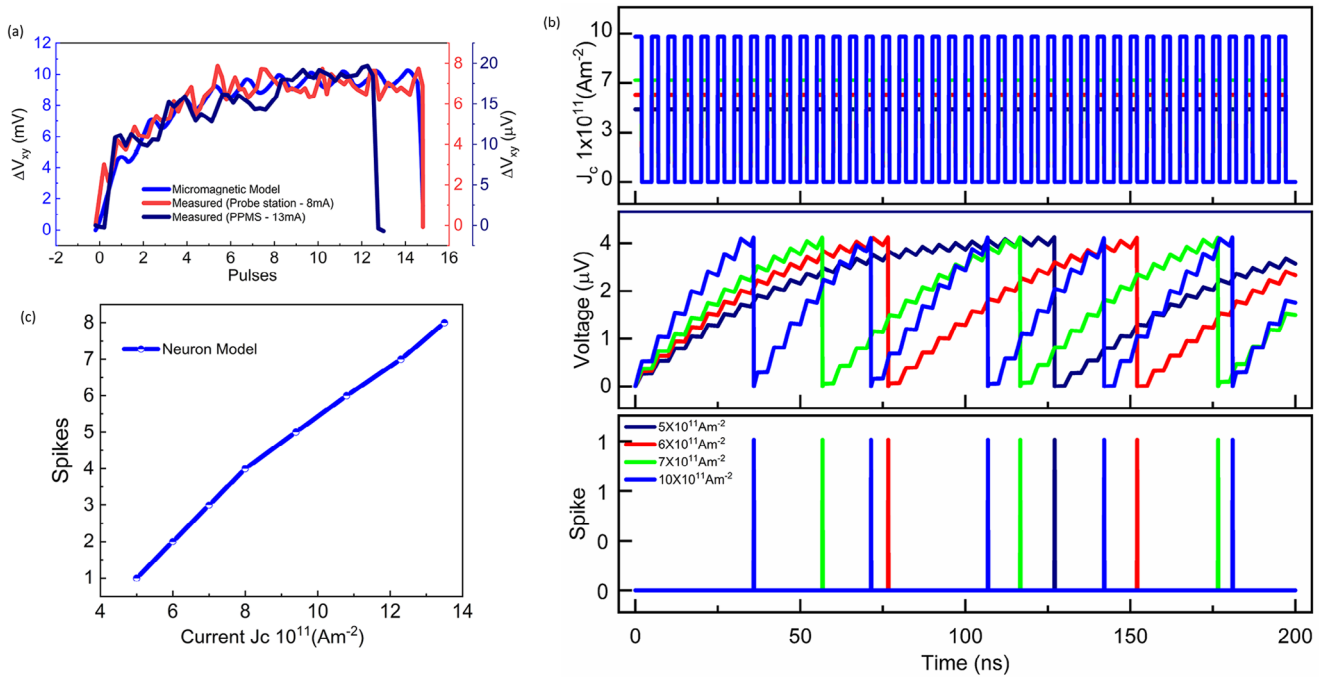


Figure 9. a) Measured LIF device characteristics and the model. b) LIF response of the model to increasing current densities shows increasing spiking frequency with increasing current density. c) Model-based results show increasing spike frequency with increasing current (simulation).

S5). As magnetization is directly related to DW position, the equation reads:

$$\frac{dm}{dt} = -\alpha_D m^2 + \beta_D + \gamma_D J(t) \tag{4}$$

Where, m is the membrane potential, threshold = 0.75, $\beta = -1e7$, $\alpha = -1.549$, $\gamma = 1.039e-3$, $J = 1e11$ and $dt = 1e-11$. Using the Equation (12) and (13), and with some algebraic modifications, the magnetization dynamics is translated into MTJ output neuron time-voltage characteristics as:

$$\frac{dV}{dt} = -\frac{1}{\tau} V^2 + \beta_D + \gamma_D J(t) \tag{5}$$

Figure 9a matches the measured LIF characteristics with the derived (proposed) LIF model, which qualitatively match each other to the accuracy above 90%. As shown, the voltage increases sharply at the beginning, and with time, the leakage component starts dominating until the voltage reaches saturation; at this point, the integration and leakage almost cancel each other out. The threshold voltage is set near the saturating point, and after that, the neuron is reset, as shown. Note: The voltage scale difference between the measured and model comes from the different reading mechanisms. Measurements (μVs) were carried out as Hall measurements, while in the proposed model, we use the MTJ reading to improve the signal; thus, the output is in the mV range. Figure 9b,c shows the spike frequency dependence on the input current in the model neuron device. Similarly to the measured current versus spike rate shown in Figure 5, the spike frequency increases with the increasing writing current density. Figure 9c shows the neuron model response regarding spike frequency to the input current amplitude. The spike frequency increases with the increasing writing current densities from 5 × 1011 Am^{-2} to 13.3 × 1011 Am^{-2}. This property shows the device can operate with the controlled spike encoding scheme. The current controlled spike encoding is demonstrated by both the model and measured (Figure 6c) devices, respectively

We adopted the SNNTorch framework[40] and integrated the measured and modeled LIF device neuron models into two types of spiking neural network architectures which include 1) Fully Connected SNN and (see **Figure** 10a) 2) Convolutional spiking neural network CSNN as shown in Figure 10b. Figure 10a shows the three-layer fully connected (FC) SNN architecture for the MNIST and Fashion MNIST data classification. The integration is carried out by using our models as the LIF neurons at each SNN node and CSNN node. The fully connected SNN comprises three- layers, with 784 input neurons, 1000 neurons in the hidden layer, and 10 neurons in the output layer. Conversely, the CSNN features two convolutional layers: Conv1 (1, 32, kernel = 5, padding = 5) and Conv2 (32, 64, kernel = 5, padding = 5), each followed by a MaxPool2d (kernel = 2, stride = 2) and the DW LIF neuron. More details have been added to the Section S6 (Supporting Information).

As shown in **Figure** 11a,d, the measured device LIF and the proposed DW-MTJ LIF models achieve a significant accuracy above 96% in all the MNIST dataset cases. Figure 11a shows the accuracy for 10 epochs for FC-SNN architecture on the MNIST dataset. The measured devices and corresponding models achieve training accuracy of around 97%, equivalent to the ideal snnLeaky model of the SNNTorch framework. Figure 11b shows the accuracy of the device models in a CSNN architecture and on the MNIST dataset. Here, the test accuracy is improved up to 97%, the same as the ideal snnLeaky model. To test the performance on the more complex dataset, in Figure 11c, the

© 2025 The Author(s). Advanced Electronic Materials published by Wiley-VCH GmbH

2199160x, 2025, 13, Downloaded from https://advanced.onlinelibrary.wiley.com/doi/10.1002/aelm.202500091 by Politecnico Di Torino Sist. Bibl Del Polit Di Torino, Wiley Online Library on [11/11/2026]. See the Terms and Conditions (https://onlinelibrary.wiley.com/terms-and-conditions) on Wiley Online Library for rules of use; OA articles are governed by the applicable Creative Commons License

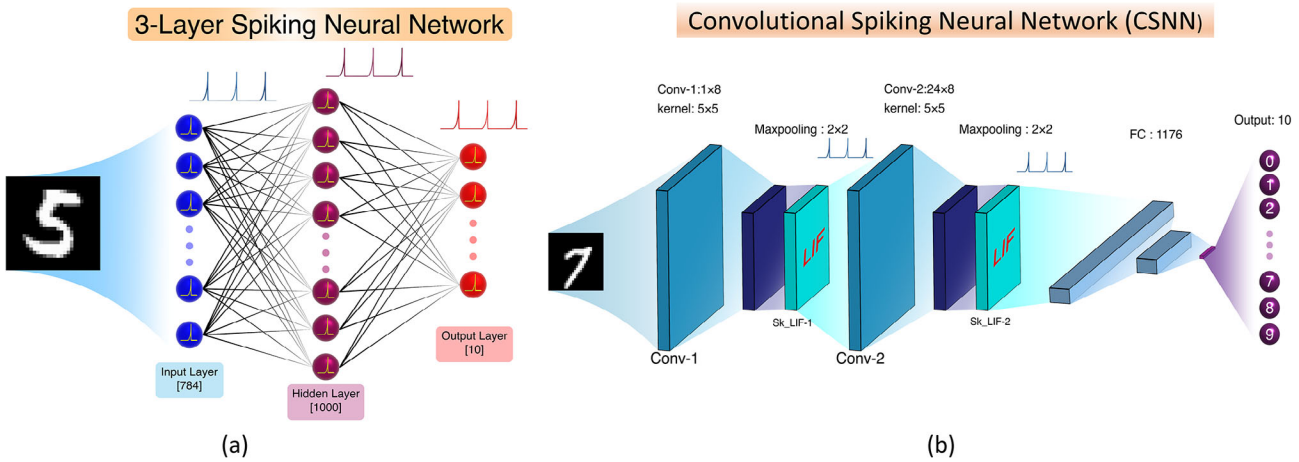


Figure 10. Neural network architectures:a) three-Layer FC-SNN with 784 input neurons, 1000 hidden neurons, and 10 output neurons. b) Convolutional-SNN (CSNN) architecture -based on the proposed neuron models.

classification accuracy on the Fashion MNIST dataset is shown. The architectures remain unchanged, as SNN and CSNN in this case. As shown, we obtained an accuracy of around 91% on the FMNIST dataset. Following training on MNIST and FMNIST, we tested our device models with test data, and compared results with snnLeaky which works as the benchmark accuracy. The proposed neuron models achieved results comparable to the ideal SnnLeaky neuron model. The full details of the classification accuracy are summarized in **Table 1**. Figure 11d shows one of the confusion matrices showing a correlation between the actual and predicted digits. In conclusion, these accuracy results, the low spike latency of the neuron, and low writing energy requirements underscore the potential of the proposed neuron models for energy-efficient neuromorphic computing applications.

In summary, by using the intricate combination of external and internal magnetic forces on the magnetic DWss, a novel spintronic LIF neuron device is demonstrated, in a multilayer ferromagnetic structure. The proposed device exhibits spintronic mem-transistor-like behavior, offering dual tunability and

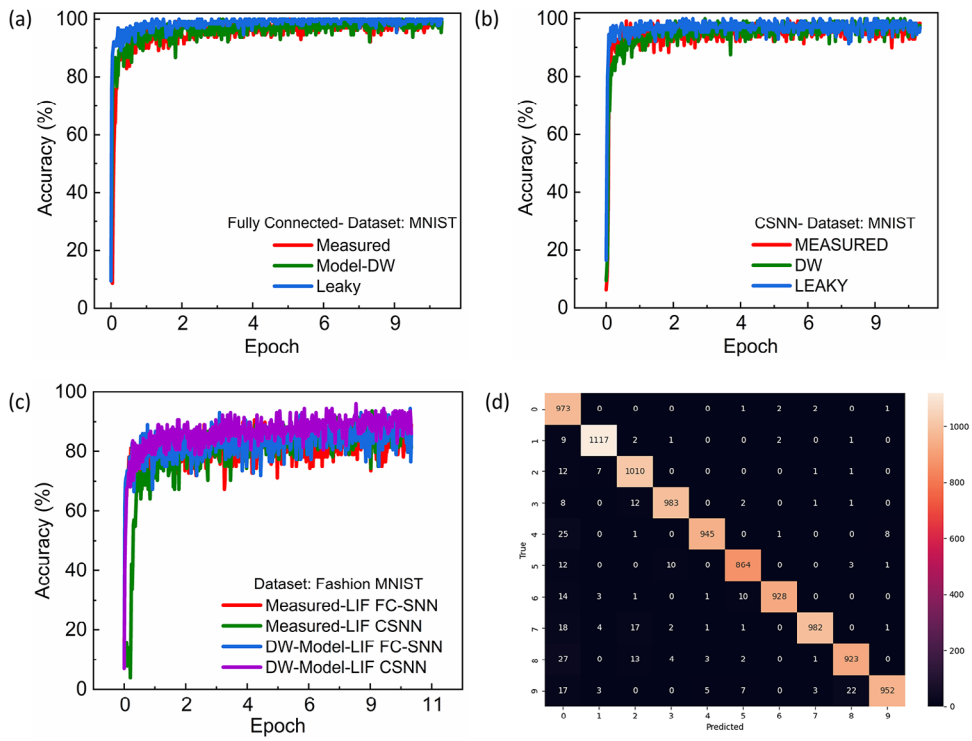


Figure 11. a) Classification accuracy on MNIST dataset in FC-SNN architecture. b)Classification accuracy on MNIST dataset in convolutional CSNN architecture. c) Classification accuracy on Fashion-MNIST dataset in FC-SNN and CSNN architecture. d) Confusion matrices.

© 2025 The Author(s). Advanced Electronic Materials published by Wiley-VCH GmbH

2199160x, 2025, 13, Downloaded from https://advanced.onlinelibrary.wiley.com/doi/10.1002/aelm.202500091 by Politecnico Di Torino Sist. Bibl Del Polit Di Torino, Wiley Online Library on [11/11/2026]. See the Terms and Conditions (https://onlinelibrary.wiley.com/terms-and-conditions) on Wiley Online Library for rules of use; OA articles are governed by the applicable Creative Commons License

Table 1. Accuracy performance matrices of the LIF models.

[b]2* Neuron model	FC-MNIST		CSNN-MNIST		FC-FMNIST		CSNN-FMNIST	
	Train accuracy (%)	Test accuracy (%)	Train accuracy (%)	Test accuracy (%)	Train accuracy (%)	Test accuracy (%)	Train accuracy (%)	Test accuracy (%)
DW-Model	97.87	96.61	96.86	96.99	84.99	83.47	88.98	90.97
Measured	97.61	96.51	96.00	97.10	89	85	89	87.67
SnnLeaky	99.28	98.11	97.28	96.79	NA	NA	NA	NA

versatility in operation. Our micromagnetic simulations predict low spike latency of around 15 ns with a writing energy of approximately 11.7 pJ per spike, making it suitable for fast neuromorphic computing applications. When integrated into FC-SNN and CSNN architectures, the device models achieve classification accuracies above 97% on the MNIST dataset and 90% on the FMNIST dataset. Additionally, the device simulations show scalability to 100×20 nm^2, which opens prospects for high-density spiking neural network hardware applications-based on these devices.

4. Experimental Section

Fabrication and Characterization: The Rotaris magnetron sputtering system deposited the magnetic thin films at room temperature on a 4-inch thermally oxidized Si wafer. A 300 nm bottom layer of SiO_2 was deposited before stack deposition by using thermal oxidization. Then, the multilayer stack was grown using ultrahigh vacuum magnetron sputtering at room temperature in 5×10^{-8} mbar. The multilayer structure consists of, from the substrate side, a 300 nm SiO_2 insulating layer. Finally, a stack of SiO_2(300 nm)/[Ta(5∼nm)/CoFeB(x)/MgO(2∼nm)] × 20 was formed, where MgO layers were deposited by RF magnetron sputtering, and the other layers were deposited by DC magnetron sputtering. After the film deposition, AZ5214 photoresist was spin-coated with a thickness of 1.6 um and performed a hard bake for 2 mins at 110°C for positive tone use. The crossbars were subsequently patterned on the resist using conventional photolithography. Ion beam etching using Ar gas removed the exposed magnetic stacks outside the resist mask. During the etching, the conductivity of the etched region was monitored, and stopped the etching when the signal from the 300-nm-thick silicon oxide layer appeared. To form electrical contacts, Ti (10 nm)/Au (100 nm) was deposited on the sides of the crossbars through sputtering at a rate of 0.8 nms^{-1}. The electrical contact pads were defined using photolithography and lifted off by immersion in acetone with ultrasonic processing for 5 min.

Characterization and Imaging: The magnetic characterization of the samples for thickness optimization was done using normal vibration sample magnetometry VSM at room temperature. After VSM, imaging of the samples with multi-domain magnetic characteristics was performed using magnetic force microscopy MFM based- Dimension Icon SPM. We used the CoIr-coated MFM tip provided by Bruker Inc. for probing. The electrical measurements were implemented in Quantum Design physical property measurement systems PPMSs Evercool II and Dynacool and a homemade probe station system equipped with an electromagnet. A Keithley model 6221 was used to source pulsed current, and a Keithley model 2182A nanovoltmeter measured the transverse voltage *Vxy*. Two pulsed currents were utilized, writing and reading pulses, with pulse widths of (500 × μs) and (12 × ms), respectively. Multiple amplitudes were used for the writing pulses, and 0.7 mA was used for the reading pulses. The transverse voltage was measured during the reading pulse, with a 2 ms delay relative to the start of the reading pulse. The measurement procedure for pulsed-current-induced transverse voltage change was as follows. Initially, a large out-of-plane magnetic field serving as a setting field (e.g., $HSet = -1800Oe$) was applied to achieve a saturated magnetization of the device. The magnetic field was then changed to a specific value defined as a bias field (e.g., $HBias = +180Oe$) to produce a magnetic multidomain state of the device, followed by ten transverse voltage recordings, each recording being the average of three individual measured voltages. Subsequently, a few writing pulses were injected to move magnetic DWs and induce Hall voltage changes. After each writing pulse, four reading pulses were applied, and four transverse voltages were recorded. Finally, the magnetic field was changed to *HSet* to reset the magnetic state of the device, and it was then reduced again to *HBias*, followed by another ten transverse voltage recordings. The timing diagram of the measurement procedure is shown below (**Figure 12**).

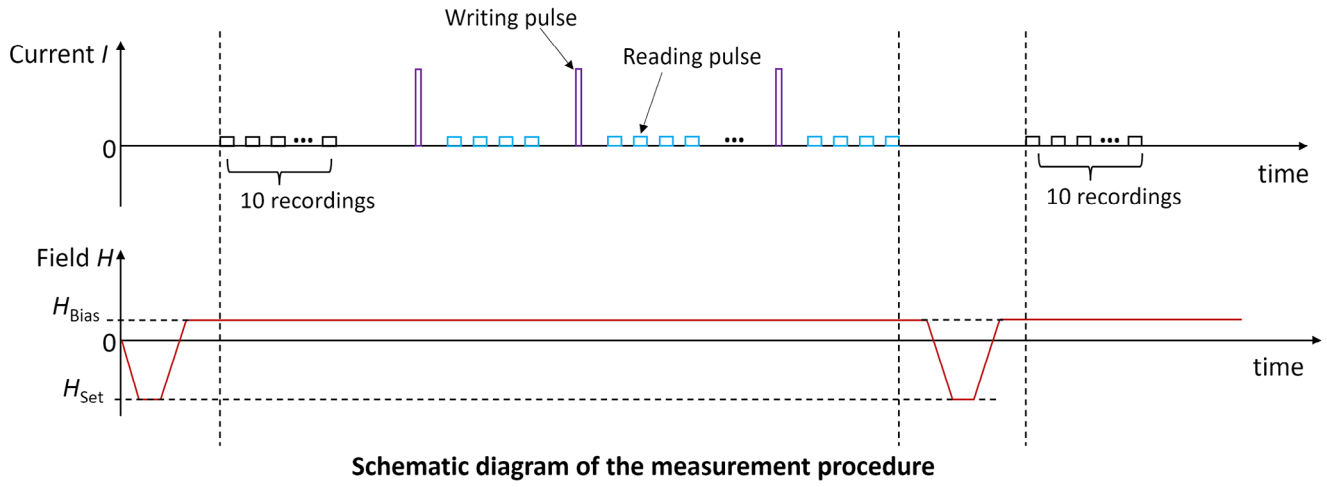


Figure 12. Measurement procedure.

© 2025 The Author(s). Advanced Electronic Materials published by Wiley-VCH GmbH

2199160x, 2025, 13, Downloaded from https://advanced.onlinelibrary.wiley.com/doi/10.1002/aelm.202500091 by Politecnico Di Torino Sist. Bibl Del Polit Di Torino, Wiley Online Library on [11/11/2026]. See the Terms and Conditions (https://onlinelibrary.wiley.com/terms-and-conditions) on Wiley Online Library for rules of use; OA articles are governed by the applicable Creative Commons License

Table 2. Details of simulated parameters.

Grid size	Cell size [nm]	Anisotropy, $\mathcal{K}_u$ ~[Jm^{-2}]	Saturation Mag, M_s [Am^{-1}]	Exchange stiffness, $\mathcal{A}$ [Jm^{-1}]	DMI, $\mathcal{D}$[?] [Jm^{-2}]	IEC, $\mathcal{J}$ [Jm^{-}2]	α_H
256, 64, X[a)]	2, 2, 0.8	0.9×10^6	0.8×10^6	1.5×10^{-11}	1.0×10^{-12}	5×10^{-13}	0.15

[a)] X is the number of layers.

5. Modelling and Simulations

The total magnetic energy of the free layer includes exchange, Zeeman, uniaxial anisotropy, demagnetization, and DMI energies.

$$E(\boldsymbol{m}) = \int_V [A(\nabla \boldsymbol{m})^2 - \mu_0 \boldsymbol{m} \cdot H_{\text{ext}} - \frac{\mu_0}{2} \boldsymbol{m} \cdot H_d - K_u(\hat{u} \cdot \boldsymbol{m}) + \varepsilon_{\text{DM}}] dv \tag{6}$$

where A is the exchange stiffness, μ_0 is the permeability, K_u is the anisotropy energy density, H_d is the demagnetization field, and H_{ext} is the external field; moreover, the DMI energy density is then computed as follows:

$$\varepsilon_{\text{DM}} = D\left[m_z(\nabla \cdot \boldsymbol{m}) - (\boldsymbol{m} \cdot \nabla) \cdot \boldsymbol{m}\right] \tag{7}$$

Solving the Euler equation yields the DWs width (δ) and the DWs energy with DMI (σ) , respectively

$$\delta = \pi\Delta = \pi\sqrt{\mathcal{A}/\mathcal{K}_{\text{eff}}} \tag{8}$$

$$\sigma = 4\sqrt{\mathcal{A}\mathcal{K}_{\text{eff}}} \mp \pi D \tag{9}$$

where $\Delta = \mathcal{A}/\mathcal{K}_{\text{eff}}$ is the Bloch wall width parameter.

Micromagnetic simulations were performed using MuMax[41,42] having the Landau–Lipschitz–Gilbert (LLG) equation as the basic magnetization dynamics computing unit. The LLG equation describes the magnetization evolution as follows:

$$\frac{d\hat{m}}{dt} = \frac{-\gamma}{1+\alpha^2}\left[\boldsymbol{m} \times \boldsymbol{H}_{\text{eff}} + \boldsymbol{m} \times \left(\boldsymbol{m} \times \boldsymbol{H}_{\text{eff}}\right)\right] \tag{10}$$

where $\boldsymbol{m}$ is the normalized magnetization vector, γ is the gyromagnetic ratio, α is the Gilbert damping coefficient, and

$$\boldsymbol{H}_{\text{eff}} = \frac{-1}{\mu_0 M_S} \frac{\delta \boldsymbol{E}}{\delta \boldsymbol{m}} \tag{11}$$

is the effective MF around which the magnetization process occurs. T The spin–orbit torque is then added in the form of modified STT in MuMax.[43]

$$\boldsymbol{\tau}_{\text{SOT}} = -\frac{\gamma}{1+\alpha^2} a_J[(1+\xi\alpha)\boldsymbol{m} \times (\boldsymbol{m} \times \boldsymbol{p}) + (\xi - \alpha)(\boldsymbol{m} \times \boldsymbol{p})] \tag{12}$$

$$a_J = \left|\frac{\hbar}{2M_S e \mu_0} \frac{\theta_{\text{SH}} j}{d}\right| \quad \text{and} \quad \boldsymbol{p} = \text{sign}\left(\theta_{\text{SH}}\right) \boldsymbol{j} \times \boldsymbol{n} \tag{13}$$

where θ_{SH} is the spin Hall coefficient of the material, j is the current density, and d is the free layer thickness. The resistance of the proposed skyrmion MTJ synapse is then computed using the compact model presented in the main discussion Equation (2). We then consider the magnetization profile of the free layer and feed it to our model, which computes the resistance of the MTJ device as follows:

$$R_{\text{syn}} = \frac{V_{\text{syn}}}{I_{\text{syn}}} \tag{14}$$

The magnetic parameters and simulation details are given in **Table 2**

Supporting Information

Supporting Information is available from the Wiley Online Library or from the author.

Acknowledgements

The authors thank King Abdullah University of Science and Technology for supporting this work. The authors also thank Camelia Florica from the nanofabrication lab for her help with the SEM imaging of the sample.

Conflict of Interest

The authors declare no conflict of interest.

Author Contributions

A.H.L. conceived the idea and fabricated the devices along with X.Z., A.H.L. and M.T. did the electrical characterization of the devices supported by D.Z. and X.Z.A.L. did the micromagnetic simulations, and neuron modeling. The neuron models were integrated into the SNN architecture by D.N.R.A.H. Lone wrote the paper with support from D.N.R.M.T., H.F, and G.S. All other authors participated in the discussion of the results. G.S. supervised the project with support from H.F.

Data Availability Statement

The data that support the findings of this study are available from the corresponding author upon reasonable request.

Keywords

domain Wall, (LIF) neuron, micromagnetics, spiking neural networks, spintronics memtransistor

Received: February 2, 2025
Revised: March 23, 2025
Published online: April 21, 2025

© 2025 The Author(s). Advanced Electronic Materials published by Wiley-VCH GmbH

2199160x, 2025, 13, Downloaded from https://advanced.onlinelibrary.wiley.com/doi/10.1002/aelm.202500091 by Politecnico Di Torino Sist. Bibl Del Polit Di Torino, Wiley Online Library on [11/11/2026]. See the Terms and Conditions (https://onlinelibrary.wiley.com/terms-and-conditions) on Wiley Online Library for rules of use; OA articles are governed by the applicable Creative Commons License

[1] D. Marković, A. Mizrahi, D. Querlioz, J. Grollier, *Nat. Rev. Phys.* **2020**, *2*, 499.
[2] A. Fert, N. Reyren, V. Cros, *Nat. Rev. Mater.* **2017**, *2*, 17031.
[3] G. Finocchio, M. Di Ventra, K. Y. Camsari, K. Everschor-Sitte, P. K. Amiri, Z. Zeng, *J. Magn. Magn. Mater.* **2021**, *521*, 167506.
[4] G. Srinivasan, A. Sengupta, K. Roy, *Sci. Rep.* **2016**, *6*, 29545.
[5] M. A. Azam, D. Bhattacharya, D. Querlioz, J. Atulasimha, *Jpn. J. Appl. Phys.* **2018**, *124*, 152122.
[6] B. Sutton, K. Y. Camsari, B. Behin-Aein, S. Datta, *Sci. Rep.* **2017**, *7*, 44370.
[7] S. Chowdhury, A. Grimaldi, N. A. Aadit, S. Niazi, M. Mohseni, S. Kanai, H. Ohno, S. Fukami, L. Theogarajan, G. Finocchio, S. Datta, K. Y. Camsari, *IEEE J. Explor. Solid-State Comput. Devices Circuits* **2023**, *9*, 1.
[8] D. Prychynenko, M. Sitte, K. Litzius, B. Krüger, G. Bourianoff, M. Kläui, J. Sinova, K. Everschor-Sitte, *Phys. Rev. Appl.* **2018**, *9*, 014034.
[9] S. S. P. Parkin, M. Hayashi, L. Thomas, *Science* **2008**, *320*, 190.
[10] Z. Luo, A. Hrabec, T. P. Dao, G. Sala, S. Finizio, J. Feng, S. Mayr, J. Raabe, P. Gambardella, L. J. Heyderman, *Nature* **2020**, *579*, 214.
[11] L. D. Landau, E. M. Lifshitz, *Phys. Z. Sowjetunion* **1935**, *8*, 153.
[12] S. Azzawi, A. T. Hindmarch, D. Atkinson, *J. Phys. D: Appl. Phys.* **2017**, *50*, 473001.
[13] I. Lemesh, G. S. D. Beach, *Phys. Rev. B* **2018**, *98*, 104402.
[14] M. Foerster, O. Boulle, S. Esefelder, R. Mattheis, M. Kläui, in *Handbook of Spintronics*, Springer, Dordrecht **2016**.
[15] W. Wang, Y. Sheng, Y. Zheng, Y. Ji, K. Wang, *Adv. Electron. Mater.* **2022**, *8*, 2200412.
[16] A. H. Lone, H. Fariborzi, *IEEE Trans. Electron Devices* **2023**, *70*, 371.
[17] K. Everschor-Sitte, J. Masell, R. M. Reeve, M. Kläui, *Jpn. J. Appl. Phys.* **2018**, *124*, 240901.
[18] K. M. Song, J.-S. Jeong, B. Pan, X. Zhang, J. Xia, S. Cha, T.-E. Park, K. Kim, S. Finizio, J. Raabe, J. Chang, Y. Zhou, W. Zhao, W. Kang, H. Ju, S. Woo, *Nat. Electron.* **2020**, *3*, 148.
[19] W. H. Brigner, N. Hassan, X. Hu, C. H. Bennett, F. Garcia-Sanchez, M. J. Marinella, J. A. C. Incorvia, J. S. Friedman, in *2022 IEEE International Symposium on Circuits and Systems (ISCAS)*, IEEE, Piscataway, NJ **2022** pp. 1189–1193.
[20] L. C., R. K. Wang C, *Sci. Rep.* **2022**, *12*, 8361.
[21] L. Liu, D. Wang, D. Wang, Y. Sun, H. Lin, X. Gong, Y. Zhang, R. Tang, Z. Mai, Z. Hou, Y. Yang, P. Li, L. Wang, Q. Luo, L. Li, G. Xing, M. Liu, *Nat. Commun.* **2024**, *15*, 4534.
[22] D. Wang, Z. Wang, N. Xu, L. Liu, H. Lin, X. Zhao, S. Jiang, W. Lin, N. Gao, M. Liu, G. Xing, *Adv. Sci.* **2022**, *9*, 2270194.
[23] L. Yang, W. Li, C. Zuo, Y. Tao, F. Jin, H. Li, R. Tang, K. Dong, *Adv. Electron. Mater.* **2024**, *10*, 2300885.
[24] T. Leonard, S. Liu, H. Jin, J. A. C. Incorvia, *Appl. Phys. Lett.* **2023**, *122*, 262406.
[25] E. Raymenants, O. Bultynck, D. Wan, T. Devolder, K. Garello, L. Souriau, A. Thiam, D. Tsvetanova, Y. Canvel, D. E. Nikonov, I. A. Young, M. Heyns, B. Soree, I. Asselberghs, I. Radu, S. Couet, V. D. Nguyen, *Nat. Electron.* **2021**, *4*, 392.
[26] B. Chen, M. Zeng, K. H. Khoo, D. Das, X. Fong, S. Fukami, S. Li, W. Zhao, S. S. Parkin, S. Piramanayagam, S. T. Lim, *Mater. Today* **2023**, *70*, 193.
[27] D. Wang, Z. Wang, N. Xu, L. Liu, H. Lin, X. Zhao, S. Jiang, W. Lin, N. Gao, M. Liu, G. Xing, *Adv. Sci.* **2022**, *9*, 2203006.
[28] H. Lin, N. Xu, D. Wang, L. Liu, X. Zhao, Y. Zhou, X. Luo, C. Song, G. Yu, G. Xing, *Adv. Intell. Syst.* **2022**, *4*, 2200028.
[29] D. Wang, Z. Wang, S. Jiang, L. Liu, H. Lin, Y. Zhang, R. Tang, X. Luo, G. Xing, *Mater. Today Electron.* **2023**, *6*, 100065.
[30] Z. Wang, D. Wang, L. Liu, S. Jiang, G. Chai, J. Cao, G. Xing, *Appl. Phys. Lett.* **2023**, *123*, 204101.
[31] F. Ponulak, A. Kasinski, *Acta Neurobiol. Exp* **2011**, *71*, 409.
[32] S. Ghosh-Dastidar, H. Adeli, *Int. J. Neur. Syst.* **2009**, *19*, 295.
[33] T. Wang, C. Shi, X. Zhou, Y. Lin, J. He, P. Gan, P. Li, Y. Wang, L. Liu, N. Wu, G. Luo, *Neurocomputing* **2021**, *425*, 96.
[34] Y. Li, Z. Xuan, J. Lu, Z. Wang, X. Zhang, Z. Wu, Y. Wang, H. Xu, C. Dou, Y. Kang, Q. Liu, H. Lv, D. Shang, *Adv. Funct. Mater.* **2021**, *31*, 2100042.
[35] C. Boretti, L. Prono, C. Frenkel, G. Indiveri, F. Pareschi, M. Mangia, R. Rovatti, G. Setti, in *2023 IEEE International Symposium on Circuits and Systems (ISCAS)*, IEEE, Piscataway, NJ **2023** pp. 1–5.
[36] G. Gallego, T. Delbrück, G. Orchard, C. Bartolozzi, B. Taba, A. Censi, S. Leutenegger, A. J. Davison, J. Conradt, K. Daniilidis, D. Scaramuzza, *IEEE Trans. Pattern Anal. Mach. intell.* **2020**, *44*, 154.
[37] S. R. Kheradpisheh, M. Ganjtabesh, S. J. Thorpe, T. Masquelier, *Neural Networks* **2018**, *99*, 56.
[38] L. H. Wang D, R. Tang, *Nat. Commun.* **2023**, *14*, 1068.
[39] D. R. Rodrigues, R. Moukhader, Y. Luo, B. Fang, A. Pontlevy, A. Hamadeh, Z. Zeng, M. Carpentieri, G. Finocchio, *Phys. Rev. Appl.* **2023**, *19*, 064010.
[40] J. K. Eshraghian, M. Ward, E. Neftci, X. Wang, G. Lenz, G. Dwivedi, M. Bennamoun, D. S. Jeong, W. D. Lu, *Proc. IEEE* **2023**, *111*, 1016.
[41] J. Leliaert, M. Dvornik, J. Mulkers, J. De Clercq, M. V. Milošević, B. Van Waeyenberge, *J. Phys. D: Appl. Phys.* **2018**, *51*, 123002.
[42] A. Vansteenkiste, J. Leliaert, M. Dvornik, M. Helsen, F. Garcia-Sanchez, B. Van Waeyenberge, *AIP Advances* **2014**, *4*, 107133.
[43] N. Nagaosa, Y. Tokura, *Nat. Nanotechnol.* **2013**, *8*, 899.

© 2025 The Author(s). Advanced Electronic Materials published by Wiley-VCH GmbH

2199160x, 2025, 13, Downloaded from https://advanced.onlinelibrary.wiley.com/doi/10.1002/aelm.202500091 by Politecnico Di Torino Sist. Bibl Del Polit Di Torino, Wiley Online Library on [11/11/2026]. See the Terms and Conditions (https://onlinelibrary.wiley.com/terms-and-conditions) on Wiley Online Library for rules of use; OA articles are governed by the applicable Creative Commons License